J. Mech. Phys. Solids 197 (2025) 106068

Contents lists available at ScienceDirect

Journal of the Mechanics and Physics of Solids

journal homepage: www.elsevier.com/locate/jmps

Grid hollow octet truss lattices that are stable at low relative density

Peijie Zhang [a], Xueyan Chen [a,*], Penghui Yu [a], Kun Zhao [b], Haoxiang Ma [c], Shiqiu Liu [d,*], Huifeng Tan [a,*], Vincent Laude [e], Muamer Kadic [e]

[a] National Key Laboratory of Science and Technology on Advanced Composites in Special Environments, Harbin Institute of Technology, 92 Xidazhi Street, Harbin, 150001, PR China
[b] Hunan Saidret Space Technology, 1288 Yunlong Road, Hunan 412000, PR China
[c] Deep Sea Engineering Division, Institute of Deep Sea Science and Engineering, Chinese Academy of Sciences, Sanya, Hainan 572000, PR China
[d] Advanced Materials Additive Manufacturing Innovation Research Center, Hangzhou City University, Hangzhou, Zhejiang 310015, PR China
[e] Université de Franche-Comté, CNRS, Institut FEMTO-ST, 25000 Besançon, France

ARTICLE INFO

Keywords:
Lightweight
Mechanical metamaterials
Energy absorption
Stable plateau stress
Grid hollow structure

ABSTRACT

Stretching-dominated lattice materials are renowned for their lightweight nature and exceptional mechanical properties. These materials, however, have historically struggled with scalability towards low relative densities at which they often exhibit unstable oscillation behavior. Here, we propose a viable solution to this issue by integrating hollow truss elements and a grid distribution into the conventional octet truss lattice. The proposed grid hollow octet truss lattices demonstrate significant improvement over the conventional octet truss lattice, with stiffness and specific energy absorption capacities respectively 25.8% and 98% larger. To quantitatively assess the stability of low relative density metamaterials, three metrics are proposed and validated. The effect on the mechanical properties of the octet lattice of the ratio of inner to outer radius and of the grid number are comprehensively investigated numerically. Numerical simulations indicate that larger geometrical parameters and grid numbers significantly enhance the stability of the octet lattice. Consequently, the proposed lattices exhibit comparable energy absorption capacity as smooth shell lattices at equivalent relative density but demonstrate a more stable nonlinear response, maintaining nearly constant stress levels at a relative density of 0.1. Experimental validation supports these findings, highlighting potential for applications to load bearing and energy absorption.

1. Introduction

Mechanical metamaterials offer a practical solution to address the urgent need for structural materials that are both lightweight and possess strong mechanical properties (Tan et al., 2022b, 2023; Yang et al., 2023; Coulais et al., 2017; Wang et al., 2022; Portela et al., 2018). Coupled with their advantageous functional characteristics, they hold promising potential for applications in acoustic absorption (Laforge et al., 2021; Cummer et al., 2016), electromagnetic absorption (Zhao et al., 2012; Oudich et al., 2024), energy absorption (Jiang et al., 2022; Chen et al., 2022; Hamzehei et al., 2023; Cao et al., 2020b; Li et al., 2021; Yu et al., 2024) and reusable energy shock-absorbing capacity (Hewage et al., 2016; Lakes and Wojciechowski, 2008; Tan et al., 2019). Recent advances in additive manufacturing techniques, such as selective laser melting and two-photon stereolithography, have enabled the precise fabrication of intricate three-dimensional structures across scales ranging from nanometers to hundreds of millimeters (Deubel et al., 2004; Kadic et al., 2012; Köhnen et al., 2018; Bauer et al., 2017). Notably, the mechanical properties of these metamaterials

* Corresponding authors.
E-mail addresses: chenxueyan@hit.edu.cn (X. Chen), liusq@hzcu.edu.cn (S. Liu), tanhf@hit.edu.cn (H. Tan).

https://doi.org/10.1016/j.jmps.2025.106068
Received 23 September 2024; Received in revised form 19 December 2024; Accepted 1 February 2025
Available online 8 February 2025

predominantly stem from the arrangement of their periodic unit cells rather than from the materials composing them. Consequently, numerous structural configurations have been devised to enhance specific material properties (Tan et al., 2022a; Dudek et al., 2023; Florijn et al., 2014; Chen et al., 2020b,a; Zhu et al., 2024).

Lattice materials, as a type of mechanical metamaterial, exhibit exceptional physical and mechanical attributes, comprising repetitive representative cells defined by three-dimensional spatial dimensions and connectivity properties (Li et al., 2018; Liu et al., 2021; Chen et al., 2024). Categorized based on joint connectivity, lattice materials can be topologically divided into bending and stretching-dominated types (Deshpande et al., 2001a). Stretching-dominated lattice materials typically demonstrate superior effective stiffness and strength compared to their bending-dominated counterparts, in direct proportion to relative density (Ashby, 2006; Cao et al., 2018, 2020a; Meza et al., 2017; Deshpande et al., 2001b), rendering them particularly well suited for lightweight applications (Al-Ketan et al., 2018).

The octet truss lattice material stands out as the most renowned stretching-dominated variant (Latture et al., 2018; Messner et al., 2015; Song et al., 2019). Deshpande et al. conducted pioneering investigations into its effective stiffness and strength, combining experimental and theoretical approaches (Deshpande et al., 2001b). Subsequently, Mohr devised a specialized small-strain formula tailored to the ideal octet truss lattice material, revealing a perpendicular plastic flow direction relative to the pressure-dependent macroscopic yield surface (Mohr, 2005). Using numerical investigations, Tancogne-Dejean et al. (2016) observed a compression response transition in octet lattice materials, shifting from an unstable torsional mode to a stable free buckling mode at a relative density of about 0.3. This observation was further experimentally affirmed by Chen and Tan (2018).

In lattice materials, the predominant method for addressing nonlinear post-buckling or unstable oscillation tendencies entails optimizing the strut cross-sections (Zhao et al., 2022), such as implementing the hollowing-out technique in solid trusses. By incorporating hollow trusses, characterized by a higher moment of inertia, the mechanical properties of the lattice material can be notably enhanced (Tancogne-Dejean and Mohr, 2018). Later, geometric hollow truss joints were further substituted with hollow spheres, resulting in significantly higher strength and energy absorption capacity compared to solid octet truss lattice materials (Bonatti and Mohr, 2017). Even with a relative density of 0.2, this structure remains stable under static pressure, constraints, and uniaxial compression. Inspired by triply periodic minimal surfaces or guided by the minimization of bending energy, a series of shell lattice structures were proposed to mitigate stress concentration around truss joints, thereby enhancing mechanical properties (Bonatti and Mohr, 2019b,a; Han and Che, 2018). As an additional point, Zhang et al. successfully achieved a notably consistent stress–strain curve with a relative density of 0.2, accomplished through meticulous optimization of the structural configuration (Zhang et al., 2023). However, the mentioned lattices lack scalability towards low relative densities. For instance, shell lattices with a relative density of 0.1 consistently exhibit unstable oscillation behavior (Bonatti and Mohr, 2019b). Thus, the pressing question remains: can nonlinear stability be achieved at lower relative densities?

In this study, we propose a feasible solution to this challenge that involves integrating hollow truss elements with a grid distribution. Through the application of the hollowing treatment to the mesh-like octet lattice, we introduce a novel class of lattice structures that we call grid hollow octet truss (GHOT) lattice, which exhibits stable nonlinear compression response at low relative density. We conduct a numerical investigation into the impact of inner and outer radius ratios and of grid numbers on the stiffness, strength, specific energy absorption, and large deformation compression response of the GHOT lattice, covering a relative density ranging from 0.05 to 0.2. Additionally, uniaxial quasi-static compression experiments are conducted on 316L stainless steel samples to validate the numerical simulations and to showcase the superior mechanical properties and ultra-stable nonlinear compression response compared to the conventional octet truss lattice.

2. Design and fabrication of metamaterials

To achieve a stable nonlinear response at a low relative density, meticulous optimization of the stress distribution within the lattice material is imperative, along with the demonstration of the efficacy of the hollow grid structure to maintain stability under large structural deformation. As depicted in Fig. 1, we integrate grids and hollow trusses, transforming solid octet truss lattice materials into two classes of hollow grid truss lattices: the conventional hollow truss lattice (HOT) and the GHOT, with grid numbers of 1 and 2, respectively. It is evident that the depicted truss-lattice cells exhibit cubic symmetry. For each relative density, five ratios of inner to outer radius are considered in this work.

Herein, the hollow parameter serves as a dimensionless coefficient that quantifies the extent of change in the hollow section, defined as

$$\alpha = \frac{R_2}{R_1}, \tag{1}$$

where R_1 and R_2 represent the outer and inner radii, respectively, of the cylindrical truss section, with each value being half of D_1 and D_2, respectively. The unit cell of the HOT lattice material comprises 36 cylindrical struts of length l. For a perfectly cylindrical rod with radius R, the first-order approximation of its relative density is

$$\overline{\rho} = 6\sqrt{2}\pi \left(\frac{R}{l}\right)^2. \tag{2}$$

Given that hollowing involves removing the internal strut lattice structure from the external lattice structure, the approximate expression for the relative density of the hollow octet truss lattice is

$$\overline{\rho} = 6\sqrt{2}\pi \left(\frac{R_1}{l}\right)^2 (1-\alpha^2). \tag{3}$$

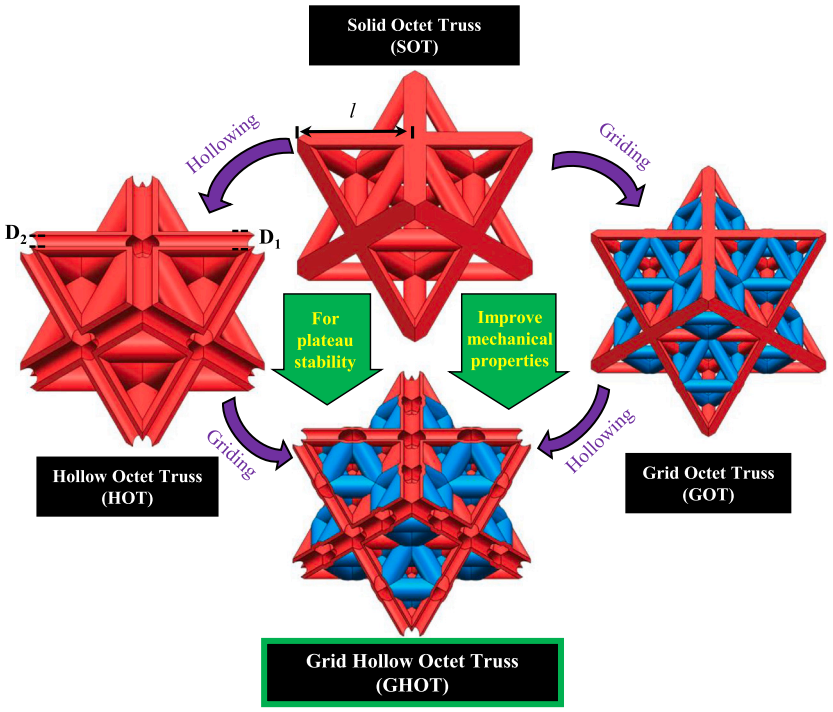

Fig. 1. General strategy for designing lightweight lattice materials with superior and stable mechanical properties. GHOT is generated through the integration of hollowing-out and grid techniques into the conventional octet truss lattice material. Notably, this design concept can be seamlessly extended to other structures dominated by stretching or bending.

Table 1
Measured dimensions and mass of the printed samples.

Type	Direction 1 (mm)	Direction 2 (mm)	Direction 3 (mm)	α	Mass (g)	Relative density (%)
SOT	29.94	29.98	29.96		45.01	20.95
	29.92	29.98	30.08		46.09	21.35
GHOT	69.99	70.28	69.97	0.58	631.21	22.92
	69.97	69.94	70.29	0.61	640.10	23.26

As the relative density increases, the impact on the relative density of the intricate shape of the joint between the rods becomes more pronounced and cannot be disregarded. A more precise estimation can be obtained by utilizing 3D computer-aided design (CAD) software, which results in

$$\overline{\rho} = C_1 \left(\frac{R_1}{l}\right)^2 (1-\alpha^2) - C_2 \left(\frac{R_1}{l}\right)^3 (1-\alpha^3), \tag{4}$$

where L is the unit cell length and the constants for the HOT lattice are $C_1 = 53.4$ and $C_2 = 155.52$. Despite GHOT featuring an increased number of struts and a triangular lattice structure in the plane, employing the same methodology allows for fitting the relative density with modified quadratic and cubic terms $C_1 = 160.36$ and $C_2 = 864$. The equations above serve as geometric constraints for the ensuing numerical simulations and sample fabrication, as illustrated in Figure **S1**. The range of densities over which the proposed approach is effective is detailed in the supplementary material. (See Note. S1)

We designed GHOT ($\alpha \approx 0.6$) metamaterials and compared them with conventional stretching-dominated SOT metamaterials. All samples were fabricated via selective laser melting of stainless steel 316L, employing a laser power of 200 W and a scanning speed of 8 m/s. Following production, a 20-min ultrasonic bath was administered to remove any residual 316L stainless steel powder. Representative samples and their unit-cells are displayed in Fig. 2. Two configurations, each with a relative density of about 0.2 and comprising $5 \times 5 \times 5$ unit cells, were examined. Two samples were prepared for each configuration to mitigate accidental errors and to ensure the universality of the results. The fabricated geometrical dimensions are detailed in Table 1. The maximum dimensional error between as-designed and measured samples is less than 0.4%.

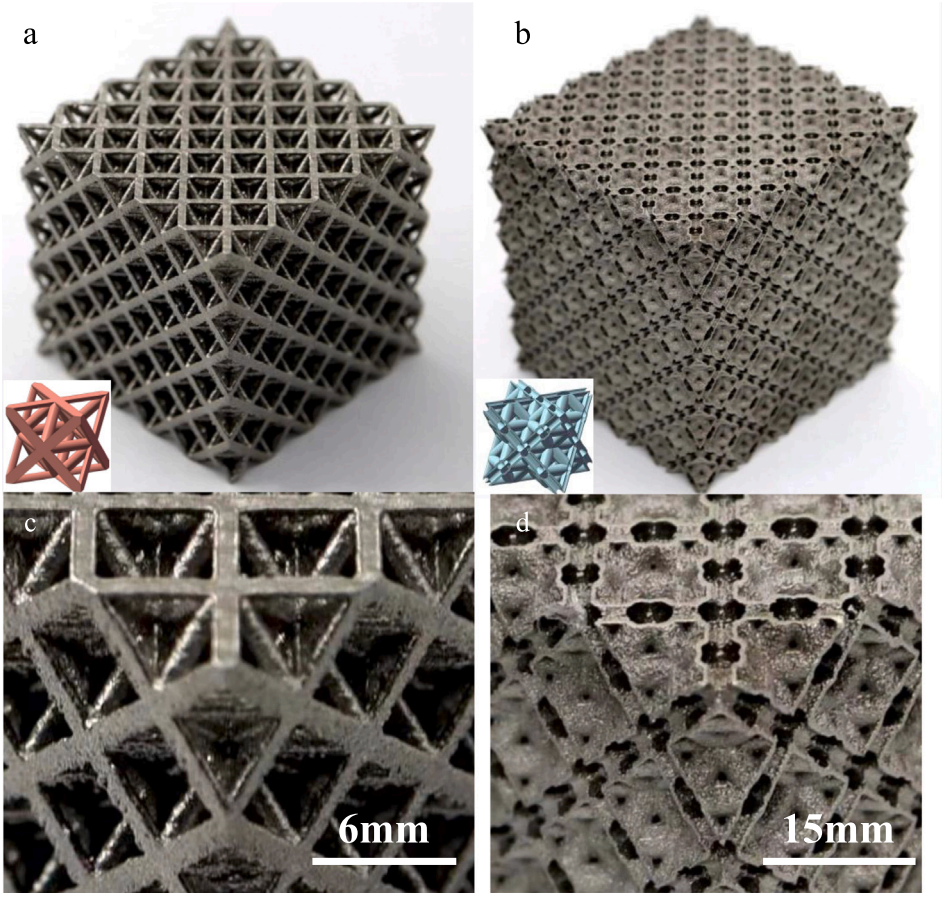

Fig. 2. Optical images of untested samples of (a) SOT and (b) GHOT, characterized by a relative density of about 0.2, that await evaluation. Zoom-in views of the SOT (c)and (d) GHOT samples are provided.

3. Experiments

By subjecting 316L stainless steel dog-bone specimens to tensile testing, we established the constitutive relationship of the base material for later use in our numerical simulations. The validity of the simulation results is confirmed through compression experiments, yielding experimental data for various configurations. The experimental procedure is outlined as follows.

3.1. Characterization of the base material

To determine the mechanical properties of the 316L stainless steel substrate, three dog bone tensile specimens were fabricated in accordance with ASTM638 standards, employing the same laser processing method used for lattice specimens. The printed dog bone specimens underwent uniaxial tensile tests at a nominal strain rate of 10^{-3} s^{-1} using a 50 kN testing machine (INSTRON5569). Axial tensile deformation was measured using a mechanically clamped extensometer. The true stress–strain curve of the tensile specimen is depicted in Figure **S3**. The average elastic modulus measures approximately 150 GPa, with an offset yield stress of 520 MPa at 0.2% strain. Fracture of the base material occurs at a strain of 0.32, corresponding to a strength of 780 MPa.

3.2. Uniaxial compression testing of lattice materials

The compression response of the test sample was examined using the MTS322 tester equipped with a 500 kN load cell, operating at a nominal strain rate of 10^{-3} s^{-1}. During testing, the sample was positioned between polished steel plates, with a suitable preload applied to prevent sliding, as illustrated in Figure **S4**. To mitigate the inherent mechanical measurement errors of the MTS322 tester, two digital cameras were employed to monitor lateral deformation, and the load–displacement curves were subsequently rectified using Vic-3D software. To ensure the accuracy of the measured data by the Digital Image Correlation code, samples were marked with a speckle pattern, featuring an average radius of approximately 45 μm. Stress is calculated by dividing the compressive force by the initial cross-sectional area of the lattice sample, while strain is determined by dividing the calibrated displacement by the

initial height of the lattice sample. To mitigate boundary effects, following the methodology utilized by Bonatti and Mohr (2017), the elastic modulus was determined by analyzing axial strain measurements collected from 8 reference points along the central row of unit cells.

4. Numerical simulations

To elucidate numerically the compression behavior of GHOT lattices, three main types of simulations were conducted: (1) Estimation of the macroscopic elastic modulus through elastic small strain analysis of uniaxial compression on the unit cell model using the Abaqus/Standard solver; (2) Determination of the large deformation response via explicit finite strain analysis of the unit cell under uniaxial compression using the Abaqus/Explicit solver, including the determination of yield strength with the Abaqus/Standard solver; (3) Assessment of large deformation stability through explicit finite strain analysis of a cubic structure composed of 27 cells under uniaxial compression using the Abaqus/Explicit solver.

Employing the commercial software Abaqus, we established a series of cell models with relative densities ranging from 0.05 to 0.2 to determine the elastic modulus and the yield strength of both HOT and GHOT materials. We employed an isotropic elasto-plastic model with isotropic hardening behavior to characterize the mechanical properties of the base materials. For 316L stainless steel, density is 7890 $\mathrm{kg/m^3}$ and Poisson's ratio is 0.3. The engineering stress–strain curve, depicted in Figure **S4**, offers comprehensive insights into the mechanical behavior of the base material. Lattice materials were meshed using first-order solid units (type C3D8R), with a minimum of 4 elements through the thickness direction for hollow trusses or 5 elements along the radius direction for solid trusses. As an illustration, considering a relative density of 0.2, to ensure calculation accuracy the following element counts were employed for meshing: 230 400 elements for SOT, 248 832 elements for HOT, 248 832 elements for GOT, and 238 080 elements for GHOT, as depicted in Figure **S5**. In all configurations, the edge length of the unit cell remains fixed at 20 mm, while the other geometrical parameters are adjusted based on the relative density. To streamline computations, the periodic boundary condition (PBC) is implemented for the cell model, with linear constraint equations utilized to align points on each pair of parallel boundary surfaces. In the case of a cubic symmetric unit cell, the linear equations for the relative boundary surface can be expressed as follows (Li, 2008)

$$u_i^{j+} = \bar{\varepsilon}_{ik}\, x_k^{j+} + u_i^*, \tag{5}$$

$$u_i^{j-} = \bar{\varepsilon}_{ik}\, x_k^{j-} + u_i^*, \tag{6}$$

where $\bar{\varepsilon}_{ik}$ denotes the average strain of the unit cell, x_i represents the coordinate of the selected point within the unit cell, u^* denotes the periodic displacement, and the superscripts $j+$ and $j-$ denote the positive and negative directions along the X axis, respectively. The correction amount u^* is applied symmetrically on the parallel opposite planes of the unit cell. Subtracting the above two equations yields

$$u_i^{j+} - u_i^{j-} = \bar{\varepsilon}_{ik}(x_k^{j+} - x_k^{j-}) = \bar{\varepsilon}_{ik}\Delta x_k^j. \tag{7}$$

The elastic modulus was determined from uniaxial compression simulations conducted at a strain of 10^{-4}. The yield strength is determined by the axial stress at the point where the permanent strain reaches 0.2%.

4.1. Large deformation compression simulation

To investigate further the potential nonlinear buckling behavior of lattice materials at low relative densities, cubic symmetric configurations composed of $3 \times 3 \times 3$ unit cells were generated with relative densities of 0.05, 0.1, 0.15, and 0.2. To ensure computational accuracy, the numerical model included at least 3 million solid elements. The numerical models were positioned between two analytically rigid surfaces, as illustrated in Figure **S5b**. Through explicit dynamic simulation, a self-contact constraint with a friction coefficient of 0.2 is applied in the model. The bottom plate remains fixed while the top plate is gradually lowered, compacting the sample by 50%. The loading speed is carefully chosen to ensure that the ratio of kinetic energy to internal energy remains below 1%.

5. Results and discussion

5.1. Stiffness and strength

Fig. 3a illustrates the impact of the inner to outer radius ratio and of the relative density on the relative modulus of GOT and GHOT materials. For all configurations, the relative modulus increases with both the relative density and the inner to outer radius ratio. Notably, when α is below 0.45, GOT and GHOT exhibit nearly identical relative modulus values. At $\alpha = 0.6$, the relative modulus of GOT and GHOT is primarily determined by the relative density. Specifically, configurations HOT and GHOT are chosen for comparison with the conventional SOT lattice. When the relative density exceeds 0.05, the power index of the elastic modulus for all configurations surpasses 1, with this trend becoming more pronounced as the inner and outer radius ratio increases. HOT demonstrates slightly greater stiffness than GHOT at low relative density, whereas the opposite holds true at high relative density. At a relative density of 0.2, the relative modulus of GHOT material is approximately 0.0466, representing a nearly 25.8% increase compared to the SOT material. Similarly, the relative modulus of a HOT material is about 0.0446, which is approximately 20.3%

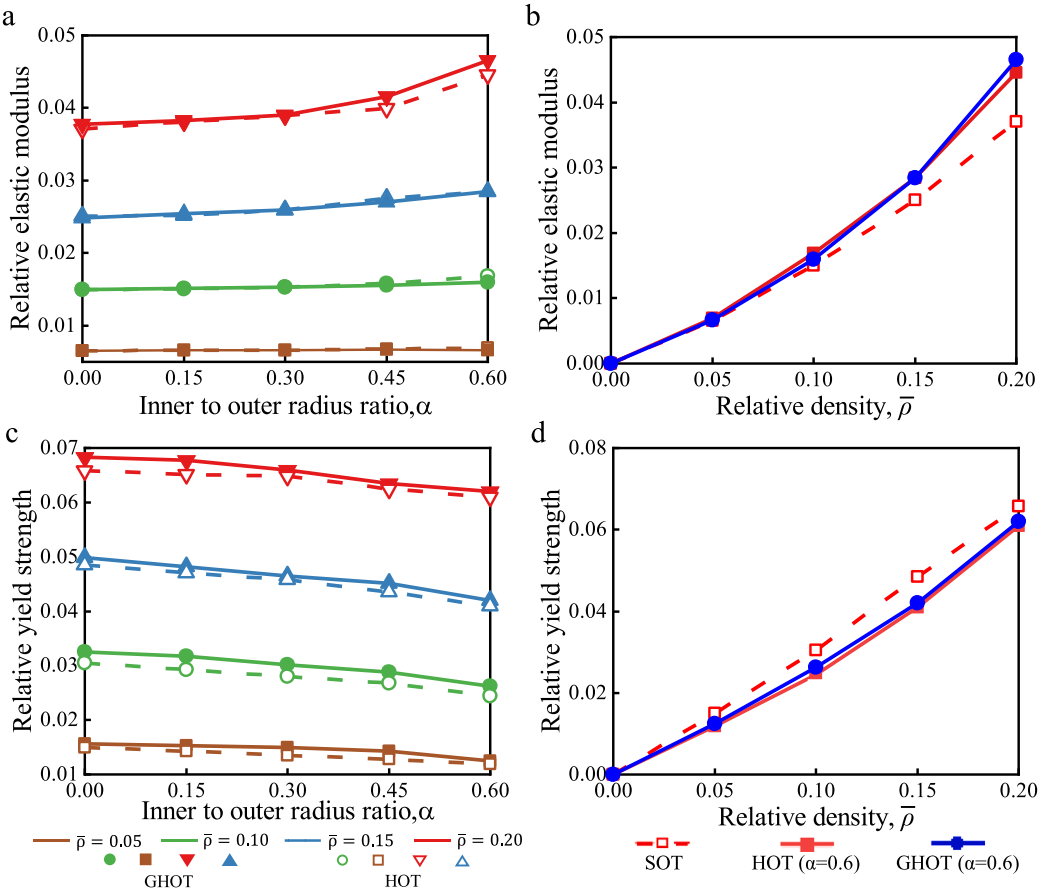

Fig. 3. (a) Evolution of the relative elastic modulus for configuration GOT and GHOT as a function of the inner to outer radius ratio. (b) Changes in the relative elastic modulus for the SOT, HOT and GHOT configurations, plotted against the relative density. (c) Trend of relative yield strength variations for GOT and GHOT in relation to the inner to outer radius ratio. (d) Comparison of the relative yield strength among GHOT, HOT, and SOT lattice materials. Relative elastic modulus means the ratio of the elastic modulus of the lattice to the base material, which is used to eliminate the influence of the base material on the lattice. A similar definition applies to the relative yield strength.

more than a conventional SOT material. This observation arises from the combined effects of the grid structure and of the hollow structure, where the outer radius of the GHOT is 113% higher than that of the GOT.

Fig. 3c illustrates the variations of the relative yield strength for configurations GOT and GHOT as a function of the inner to outer radius ratio. For all relative densities, the relative strength of GHOT consistently surpasses that of HOT for the same inner to outer radius ratio, owing to the deformation mechanism of the grid structure. At low and medium relative densities, the hollowing treatment significantly enhances the resistance of lattice structures to both linear and nonlinear buckling by extending plastic strain before the initial peak stress, thereby softening the plastic compression response of lattice structures. However, the enhancement from the grid structure is limited and cannot fully compensate for the effect of the hollowing treatment. Consequently, the relative yield strength exhibits a slight downward trend with increasing inner to outer radius ratio.

5.2. Large deformation simulation

The stress–strain curves and deformation sequences of lattice materials with relative densities 0.05, 0.1, 0.15, and 0.2, obtained through multi-cell simulation, are presented in Figs. 4–6. All lattices exhibit a similar linear behavior in the elastic region. The subsequent nonlinear region of the compression response strongly correlates with the inner and outer radius ratio as well as with the relative density.

Nonlinear buckling failure dominates at low relative densities. Specifically, at a relative density of 0.05, all HOT and GHOT lattices demonstrate an initial peak stress, followed by buckling oscillations and collapse in a layer-by-layer manner. It is evident that GHOT lattices with larger α and grid numbers exhibit buckling oscillations with reduced damping and longer periods. As depicted in Fig. 4b, unlike other lattices, the GHOT lattice (α = 0.6) shows a notably uniform deformation pattern, albeit local buckling occurring around the middle part. This results in a higher peak stress and a relatively stable curve when the applied strain

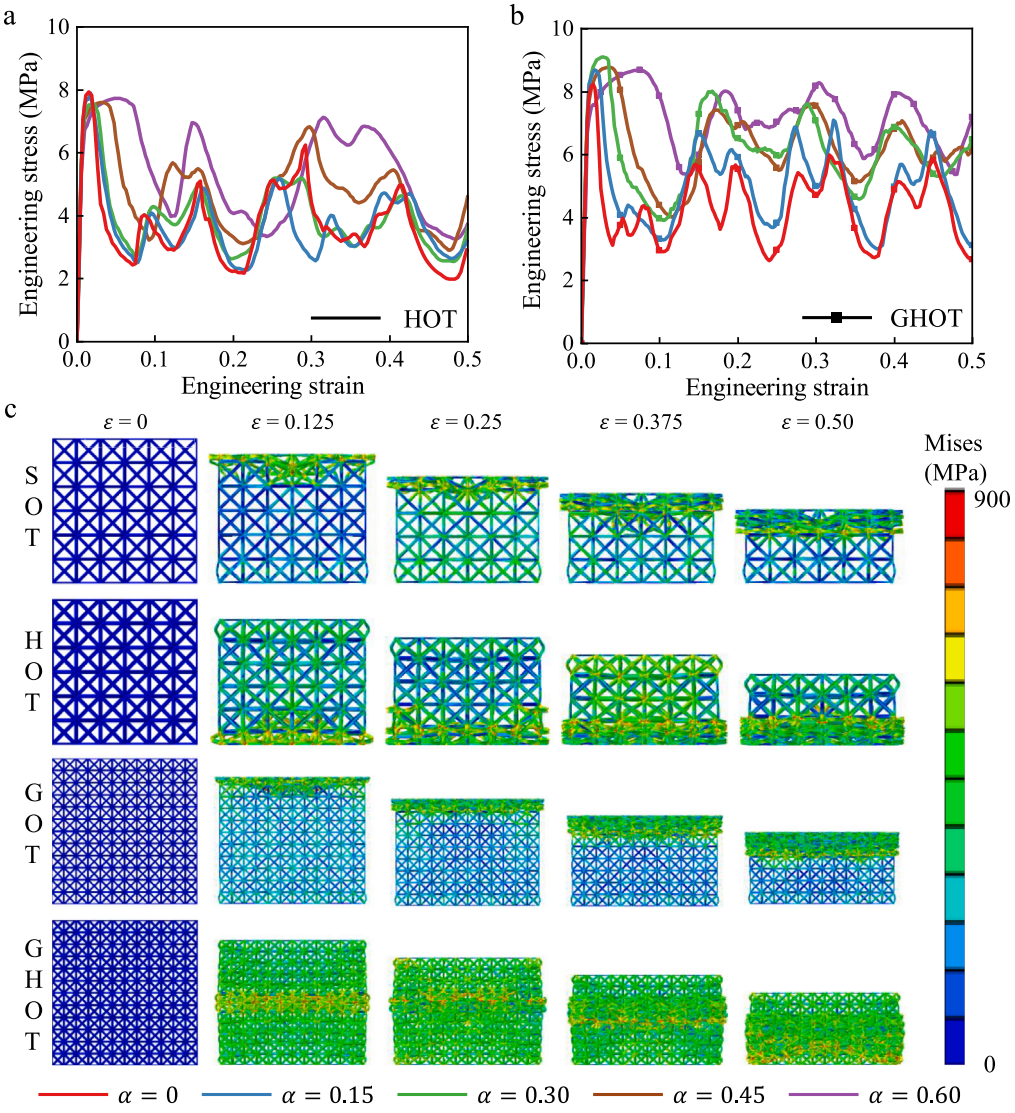

Fig. 4. Numerical simulation results for multi-cell structures with a relative density of 0.05: (a, b) Uniaxial stress–strain curves of HOT and GHOT lattices under uniaxial compression. (c) Selected stress deformation patterns with stress contour for SOT, HOT, GOT ($\alpha = 0.6$) and GHOT ($\alpha = 0.6$).

falls between 0.15 and 0.3. This observation also highlights the influence of both grid structure and hollow architecture on the stability of the stress–strain curve at low relative density, that becomes more pronounced at 0.1 relative density.

At a relative density of 0.1, the deformation mode of the SOT remains unchanged. Each layer collapse is accompanied by a rapid decrease in stress value (See Figure **S6**). Conversely, the HOT structure, despite exhibiting the same failure mode of laminar collapse, presents a distinctly different compression response. This disparity arises from the increased pole moment of inertia of the strut due to the hollow member, ensuring uniform deformation across the structure for overall load bearing. Consequently, even with the same failure mode, the stress value stabilizes relatively. Additionally, in GOT and GHOT lattices, large deformation leads to the emergence of an X-shaped stress concentration shear band. The incorporation of grid and hollow structures in GHOT lattice fosters more uniform deformation, resulting in a stress–strain curve with a hardening slope close to zero – a characteristic not typically observed in other stretching-dominated truss, shell, and plate lattices.

At relative densities of 0.15 and 0.2, the SOT lattice continues to exhibit noticeable oscillations (See Figs. 5, 6 and S7). As the inner and outer radius ratio increases, the oscillation amplitude decreases. When this ratio reaches 0.60, the stress–strain curve of the HOT lattice at both relative densities exhibits a slight oscillatory behavior, with a non-zero hardening slope. Similarly, the GOT lattice shows no significant buckling oscillation at a relative density of 0.2, presenting a large deformation response akin to a stress platform. Likewise, the stress hardening slope of the GHOT lattice with an inner to outer radius ratio between 0 and 0.6 approaches zero. Notably, the stress amplitudes consistently surpass those of the HOT lattice at equivalent relative densities, with deformation across all GHOT configurations exhibiting uniformity.

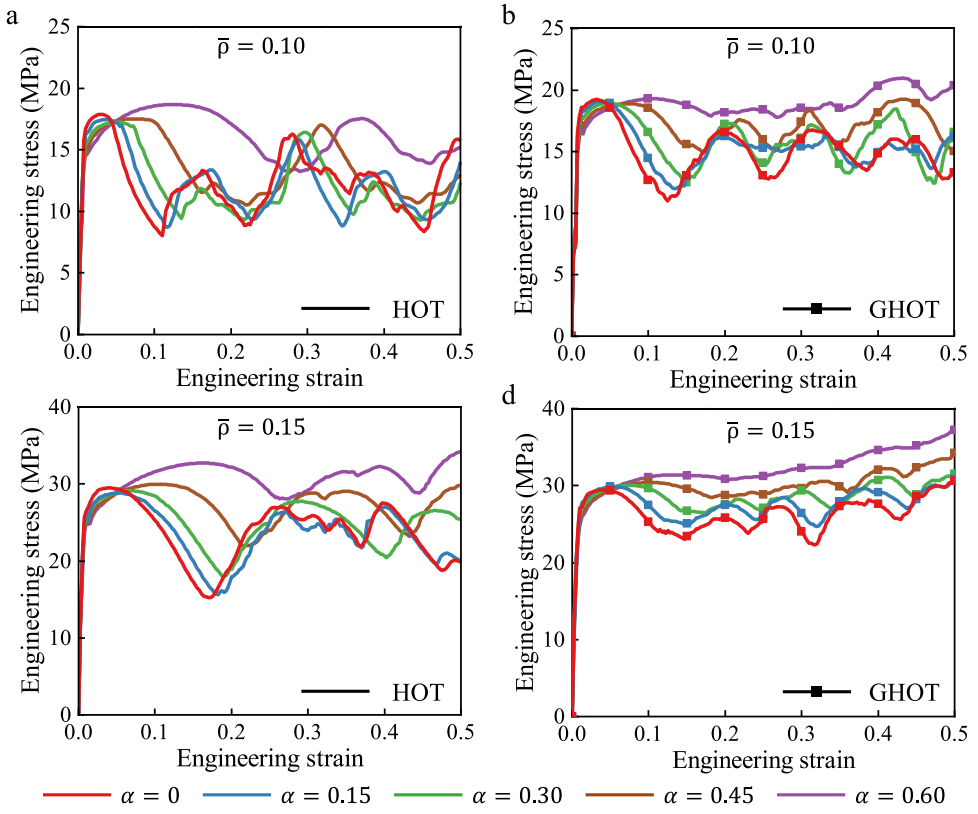

Fig. 5. Numerical simulation results of multi-cell structures with a relative density of 0.1 and 0.15: (a–d) Uniaxial stress–strain curves of HOT and GHOT lattices under uniaxial compression.

To delve into the underlying deformation mechanisms and to investigate the impact of grid and hollow structures on stress stability during compression, we conducted a series of additional quasi-static simulations on unit cell models of SOT, HOT, GOT, and GHOT lattices. For the relative densities considered in this paper ($\rho \leq 0.2$), the overall bearing capacity of the SOT lattice decreases due to the buckling (either elastically or plastically) of the struts in a layer-by-layer fashion (See Figs. S8 and S9). This buckling behavior of the struts prevents the lattice from functioning stably as a support. Moreover, due to the pillar buckling phenomenon, the other struts in the same layer are less able to bear the load, leading to further buckling and the formation of a buckling layer. This buckling behavior compromises the lattice's ability to function stably as a support. Furthermore, due to the pillar buckling phenomenon, the remaining struts in the same layer are less capable of bearing the load, resulting in additional buckling and the formation of a buckling layer. Interestingly, an asymmetric twisting buckling mode was identified at low relative densities through unit cell simulations in Tancogne's study (Tancogne-Dejean et al., 2016), which appears to contradict our results (See Fig. S8). This discrepancy arises because imperfections were introduced into the reduced numerical model. However, the potential imperfections or flaws induced during fabrication remain uncertain and cannot be identified prior to a compression test. In the absence of such defects, a symmetric layer-by-layer buckling mode is observed (as shown in Fig. S8b), consistent with the multi-cell simulation results. This behavior is further confirmed by the interlaminar collapse phenomenon observed in the multi-cell simulations of both Tancogne's work (Tancogne-Dejean et al., 2016) and this manuscript (see Figs. S10). This scenario inevitably results in a reduction of the compressive response and effectively explain the failure mechanism associated with the low aspect ratio of the struts (r/l). The buckling oscillation in the compression response gradually diminishes as the relative density increases (See Figs. 4–6).

Similarly, the elastic or plastic buckling of the struts results in the failure of the GOT lattices. After a relatively stable global deformation, GOT lattices experience localized layer collapse. This collapse behavior should be more serious due to their slender struts. Interestingly, the deformations of GOT lattices appear more uniform compared to those of SOT lattices. This can be attributed to the grid working mechanism, which confines the crushing collapse behavior to specific layers of the grid structure, progressing in multiple stages (See Figs. S9, S11–S13). This staged collapse reduces the stress levels associated with inter-layer failure, resulting in a more stable stress response. Additionally, the localized effects of buckling dissipate quickly due to subsequent densification within the affected layers. In other words, the integration of the grid structure enhances stress distribution across layers while maintaining the performance of individual layers. By introducing the grid working mechanism, the overall load-bearing capacity of the octet lattice is significantly improved.

It is evident that HOT lattices also experience significantly reduced layer-by-layer collapse failure caused by the buckling of hollow struts, in contrast to SOT and GOT lattices (See Figs. S9, S11–S12). The enhanced buckling resistance of HOT lattices stems

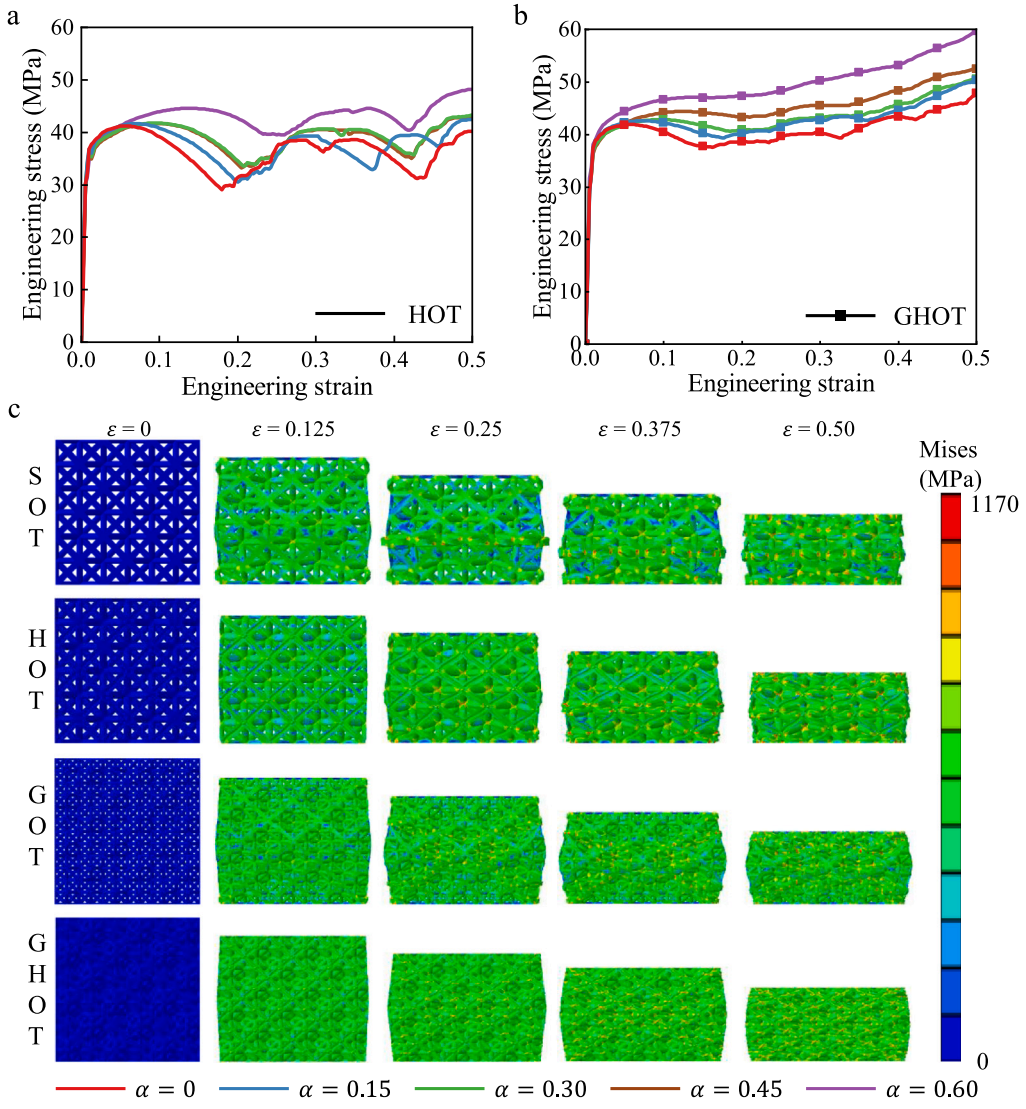

Fig. 6. Numerical simulation results of multi-cell structures with a relative density of 0.2: (a, b) Uniaxial stress–strain curves of HOT and GHOT lattices under uniaxial compression. (c) Selected stress deformation patterns with stress contour for SOT, HOT, GOT ($\alpha = 0.6$) and GHOT ($\alpha = 0.6$).

from their hollow struts, that boast larger inertia moments. A sufficiently large outer radius of the truss expedites the densification stage while maintaining ample resistance against truss buckling and instability, thereby rapidly bolstering structural stiffness. However, even for an inner and outer radius ratio of 0.6, the HOT lattice still succumbs to interlayer collapse at a relative density of 0.2 (See Fig. 6). In contrast, the GHOT lattice, formed by integrating hollow struts with grid distribution, showcases uniform deformation without interlayer collapse at a relative density no less than 0.1 under significant deformation. Unsurprisingly, at low relative densities, strut buckling dominates the failure of the GHOT lattice. Interestingly, the grid network distribution confines buckling to a specific layer, while the hollow treatment ensures the stiffness of other layers. The subsequent self-contact of the struts enhances the compression response, making it smoother than in other lattices. As the relative density increases to 0.1, the coupling mechanism strengthens the struts, enabling them to resist buckling. The failure mechanism of the GHOT lattice shifts from interlayer collapse to overall deformation and densification, stabilizing the structure's bearing capacity due to changes in the deformation regulation and failure mechanism. Such commendable stable nonlinear response positions it as a promising material for energy absorption and load bearing applications.

To further substantiate our perspective, we compare the deformation mechanisms and performance of our lattices with other strategies for creating architected materials exhibiting delocalized plastic deformations, such as nanoscale tubes (Schaedler et al., 2011; Zheng et al., 2014), disordered structures (Hooshmand-Ahoor et al., 2024, 2022; Tarantino et al., 2019), sequential buckling (Frenzel et al., 2016; Liu et al., 2024), and plate-and-shell designs (Tancogne-Dejean et al., 2018; Guell Izard et al., 2019). Nanoscale lattice (Schaedler et al., 2011) demonstrates exceptional mechanical performance at very low wall thickness

ratios, which aligns with our findings: thinner wall thicknesses at the same relative density enhance mechanical properties during large deformation. However, despite their thin walls, rapid collapse occurs due to truss buckling during the compression of hollow truss members, leading to a significant loss of stability during large deformation stages (Figs.S14a and c). This highlights that improving mechanical properties solely through thinner walls, without modifying the structural design, compromises the stability of the stress–strain curve and increases the complexity of the fabrication process. Additionally, the Ashby plot (Zheng et al., 2014) shows that micro- and macro-scale octet lattices exhibit similar mechanical properties at the same relative density (0.1) (Fig. S14b), indicating a minimal size effect for such structures. When stiffness and strength are comparable, the GHOT lattice offers superior stress stability during large deformation. For disordered structures (Hooshmand-Ahoor et al., 2024, 2022; Tarantino et al., 2019), their elastic modulus and yield strength slightly surpass those of the GHOT lattice. However, these disordered structures primarily fail through fracture zones extending across the entire specimen (in 2D structures, see Fig. S15c) and plastic localization in non-connected regions (in 3D structures, see Fig. S15d). During large deformation, their unique design results in relatively weak uniform deformation behavior under uniaxial compression (see Fig. S15). This leads to stress oscillations and a reduction in load-bearing capacity during the large deformation stage. Moreover, the optimal application range for disordered structures is within medium relative densities. At low relative densities, fabricating disordered structures becomes increasingly difficult (see Fig. S15b). Different from other lattices, sequential buckling structures (Frenzel et al., 2016; Liu et al., 2024) take advantage of buckling behavior for enegy absorption. For sequentially buckling structures, there are significant stress oscillations as strain increases (as shown in Fig. S16a), which severely hinder the energy absorption performance of the structure. Specifically, the ‘‘embrace buckling’’ concept in these structures leads to overall instability, primarily caused by excessive plastic strain at the weakly connected points (as shown in Fig. S16b), which results in a decline in mechanical properties. Consequently, sequential buckling structures exhibit significantly weaker mechanical properties, such as elastic modulus, yield strength, and specific energy absorption, compared to GHOT lattices (as shown in Fig. S16c). Plate and shell lattices are structures that effectively combine strength and stiffness at medium and high relative densities (Tancogne-Dejean et al., 2018; Guell Izard et al., 2019; Tancogne-Dejean et al., 2019). However, at low relative densities, during the large deformation stage, the mechanical behavior of both plate and shell lattices is significantly constrained by phenomena such as plate buckling and shell buckling (see Fig. S17). For instance, the plate lattice (Tancogne-Dejean et al., 2019) exhibits considerable stress oscillations (due to thin wall plate buckling) even at a relatively high density of 0.22, leading to a significant decline in mechanical performance during large deformation. Worse still, as the relative density decreases, plate lattices experience more pronounced oscillations during the nonlinear stage, with a nonlinear decrease in specific energy absorption. Consequently, while plate lattices are stiffer and stronger than GHOT lattices, they exhibit poorer specific energy absorption and mechanical properties during large deformation (see Fig. S17c). The shell lattice (Guell Izard et al., 2019), constructed from brittle-like materials, transitions to a ‘‘brittle fracture’’ failure mode when the relative density exceeds 0.25. At lower relative densities, its failure mechanism shifts to a ‘‘layer-by-layer’’ mode. To isolate the influence of the base material, the normalized strength is compared. At a relative density of 0.15, the plateau stress of the shell lattice is only 0.0132 times the yield strength of the base material. In contrast, the GHOT lattice achieves a plateau stress that is 0.064 times the yield strength of the base material at the same relative density. Additionally, the shell lattice proposed in Guell Izard et al. (2019) continues to exhibit significant deformation oscillations—an issue commonly encountered by plate and shell lattices at low relative densities. Through a comprehensive comparison of the four design methods discussed above, we have found that each approach embodies its own unique design philosophy. However, in terms of stress stability during the large deformation stage, our design philosophy outperforms the others.

5.3. Specific energy absorption

For lattice materials, specific energy absorption (SEA) quantifies the mechanical work (per unit mass) required to deform a material to 50% strain under a uniaxial load.

$$\mathrm{SEA} = \frac{\int_0^{0.5} \sigma d\varepsilon}{\rho} \tag{8}$$

The progression of SEA concerning relative density is depicted in Fig. 7. Notably, SEA for all configurations exhibits a monotonically increasing trend with the inner to outer radius ratio and the grid number. Additionally, SEA correlates positively with relative density, indicating that a higher mass of the base material enhances specific energy absorption capacity. Results indicate that a larger inner to outer radius ratio and grid number not only reduce nonlinear post-buckling response but also augment the SEA of the octet truss lattice. Particularly noteworthy, among all relative densities explored, the GHOT lattice with $\alpha = 0.6$ demonstrates the most stable nonlinear response, leading to the highest strain energy absorption, surpassing SOT lattice materials under identical relative densities by factors of 98%, 52%, 35%, and 36%, respectively. This can be attributed to the robust resistance against buckling provided by the hollow truss, that is particularly prominent at low relative densities. Subsequent integration of grid lattice structures further enhances and stabilizes resistance against extensive deformation during compression.

5.4. Evaluation of nonlinear stability for lattice materials

The compressive stress–strain curve of lattice materials typically manifests in three distinct stages: the initial elastic region, a substantial plastic deformation stage, and a final densification phase. As energy-absorbing materials, particular emphasis is placed on the plastic large deformation stage. The nonlinear response of the lattice can be categorized into either enhanced-type or fluctuated-type, each with ideal representative curves (see Fig. 8a). For energy-absorbing applications, the enhanced-type is more desirable.

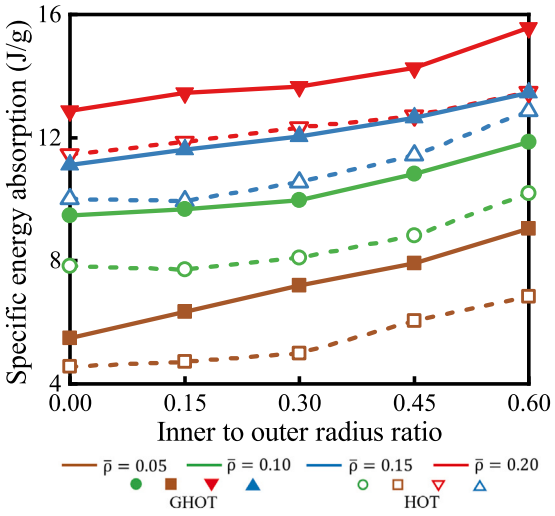

Fig. 7. Evolution of specific energy absorption of lattice materials as a function of the inner to outer ratio.

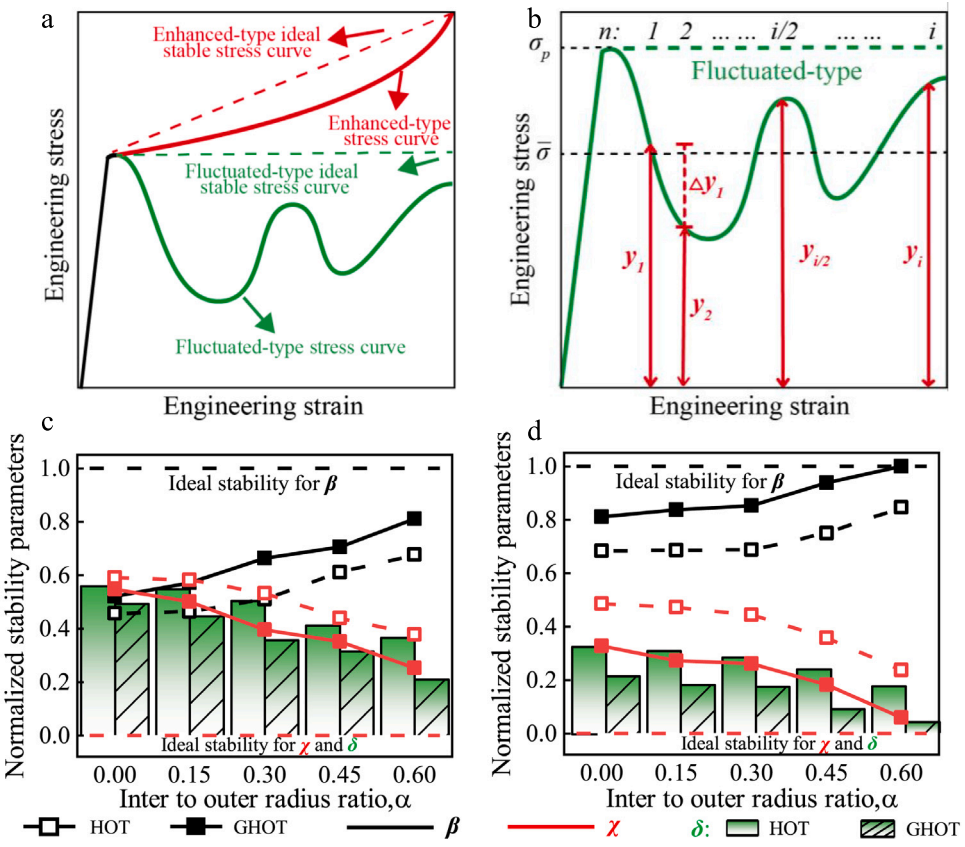

Fig. 8. (a) Fluctuated-type and enhanced-type stress–strain curves, along with the corresponding ideal stress curve. (b) Parameters used in the formulas for stability metrics. The expression for the stability parameter of the stress–strain curve for GHOT and HOT lattices at relative densities of (c) 0.05 and (d) 0.10.

However, at low relative density, local or global buckling behavior predominantly governs the deformation of the lattice materials. Consequently, the compressive stress–strain curve primarily reflects the fluctuated type, which constitutes the primary disparity in energy absorption. To quantitatively assess the stability of low relative density metamaterials, three metrics are proposed herein.

(i) Average Plateau Stress Ratio (β) – This metric serves two purposes. Firstly, it distinguishes between enhanced-type and fluctuated-type stress curves, sine theoretically the curve is enhanced when $\beta > 1$. Secondly, it reflects data dispersion to some extent. The ratio β, defined as the average stress to the initial peak stress, is used to evaluate nonlinear stability. When the ratio is close to 1, the stress plateau is more pronounced. By definition,

$$\beta = \frac{\overline{\sigma}_{\text{ave}}}{\sigma_{\text{peak}}} \tag{9}$$

with

$$\overline{\sigma}_{\text{ave}} = \frac{\sum_{n=1}^{i-1}[(\varepsilon_{n+1} - \varepsilon_n)(\sigma_{n+1} + \sigma_n)]}{2(\varepsilon_n - \varepsilon_1)} \tag{10}$$

where $\overline{\sigma}_{\text{ave}}$ denotes the average stress of the plateau, σ_{peak} signifies the initial peak stress, and n represents the number of points on the stress–strain curve.

(ii) Improved Standard Deviation (δ) – This metric reflects the discrete relationship between the true stress values and the average stress value. When δ tends to 0, the degree of data dispersion is minimized. By definition,

$$\delta = \sqrt{\frac{1}{n}\sum_{n=1}^{i}\left(\frac{\sigma_n}{\overline{\sigma}_{\text{ave}}} - 1\right)^2}. \tag{11}$$

The above two evaluation criteria both reflect the degree of data dispersion, indicating the extent of stress value variation. However, they do not adequately account for the fluctuation degree of the curve, specifically ignoring the influence of strain in the curve.

(iii) Fluctuation Coefficient (χ) – Given the challenge of achieving sustained stress increase in the plateau area under low relative density conditions, a volatility-based formula is employed to assess curve stability (as elaborated in this paper, the fluctuation coefficient is calculated when $\beta \leq 1.02$, with a set 2% deviation). When the fluctuation coefficient is close to 0, the stress curve is deemed highly stable. By definition,

$$\chi = 1 - \left[1 - \sum_{n=1}^{i-1}\left(\frac{\varepsilon_{n+1} - \varepsilon_n}{\varepsilon_n - \varepsilon_1}\frac{|\frac{\Delta\sigma}{\Delta\varepsilon}|_n}{|\frac{\Delta\sigma}{\Delta\varepsilon}|_{\max}}\right)\right]\beta \tag{12}$$

where $|\frac{\Delta\sigma}{\Delta\varepsilon}|_n$ is the absolute slope between two adjacent points, and $|\frac{\Delta\sigma}{\Delta\varepsilon}|_{max}$ represents the maximum gradient between any two adjacent points across all curves of the same relative density being compared, as illustrated in Fig. 8b.

Fig. 8c,d illustrates the fluctuation of the stress–strain curve for HOT and GHOT lattices using three different normalized parameters. It is evident that as relative density increases, β of the curve increases while χ decreases, indicating that the curve tends to become more stable. Additionally, the fluctuation of the curve stabilizes with increasing inner-to-outer diameter ratios or grid numbers, aligning with the intuitive behavior observed in the stress–strain curves shown in Figs. 4–6. For the GHOT lattice, when the relative density is 0.1 and the inner-to-outer diameter ratio is 0.6, the average plateau stress ratio of the GHOT lattice is approximately 1, reaching the optimal value of the fluctuated-type curve. Additionally, χ is only 0.05, approximately 1/10 of that of the SOT lattice. Notably, when the relative density exceeds 0.1, increasing the geometrical ratio can result in the over-stabilization of the GHOT lattice (see Figure **S18**). Specifically, at a relative density of 0.15, the GHOT lattice with $\alpha = 0.6$ transitions from a fluctuated-type to an enhanced-type. At a relative density of 0.2, more GHOT lattices undergo this transformation, while the HOT lattice remains in a fluctuating state, albeit the $\alpha = 0.6$ variant being more stable than the solid grid lattice. These results suggest that at low relative densities, not only does the mechanical failure mode change, leading to improved performance of the original structure in the nonlinear stage, but the changes in the stability of the hollow grid structure also contribute to enhancing the bearing efficiency. Upon reaching medium relative densities, the GHOT lattice shifts from fluctuated-type to enhanced-type, addressing the issue of reduced truss structure carrying capacity due to stress fluctuations.

To further confirm that our design strategy effectively stabilizes the stress curve in the region of low relative density, we compared it with other lattices at the same relative density ($\overline{\rho} = 0.1$), as shown in Fig. 9. The $\delta-\beta$ and $\chi-\delta$ curves are used to assess the stability of the stress curve, with ideal stable points at coordinates $(1, 0)$ and $(0, 0)$, respectively. It is observed that the fluctuation coefficient changes significantly even when the average stress and the improved standard deviation are similar across different lattices (see the enlarged portion in Fig. 9a). This highlights the inadequacy of evaluating stability using only one or two parameters. Among all the compared lattices, the GHOT lattice is closest to the two optimal stable points and performs better in all three parameters used to assess stability. This indicates that the GHOT lattice exhibits superior stability compared to the other lattices at a 0.1 relative density. The addition of a grid hollow structure significantly enhances the stability of the compressive response compared to plate and shell lattices, contributing to improved energy absorption efficiency at low relative densities.

5.5. Comparison between experiment and simulation

Fig. 10 summarizes the compressive stress–strain curves of different specimens along with the corresponding deformation frames. Solid lines represent the experimental results, while dashed lines represent the simulation predictions. The experimental results agree well with the numerical results in terms of elastic modulus, yield strength, and $SEA_{50\%}$ (the energy absorbed by 50% compression deformation), despite the actual sample consists of $5 \times 5 \times 5$ cells whereas only $3 \times 3 \times 3$ cells are considered in the simulation. The numerical simulation successfully captures the deformation mechanism and buckling oscillations observed in the SOT lattice

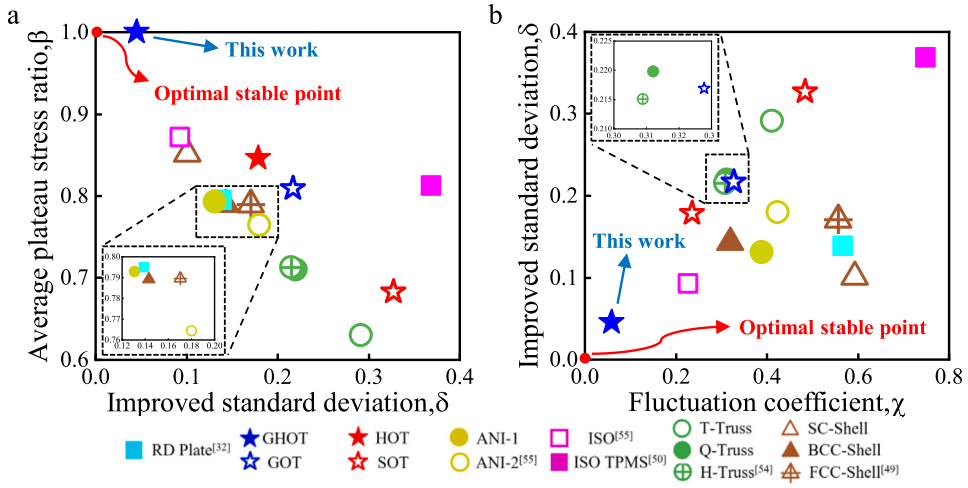

Fig. 9. Comparison of the proposed GHOT lattice with other conventional bending-dominated and stretching-dominated truss and shell lattices in terms of nonlinear stability (Chen et al., 2024; Bonatti and Mohr, 2019b,a; Li et al., 2020; Duan et al., 2020).

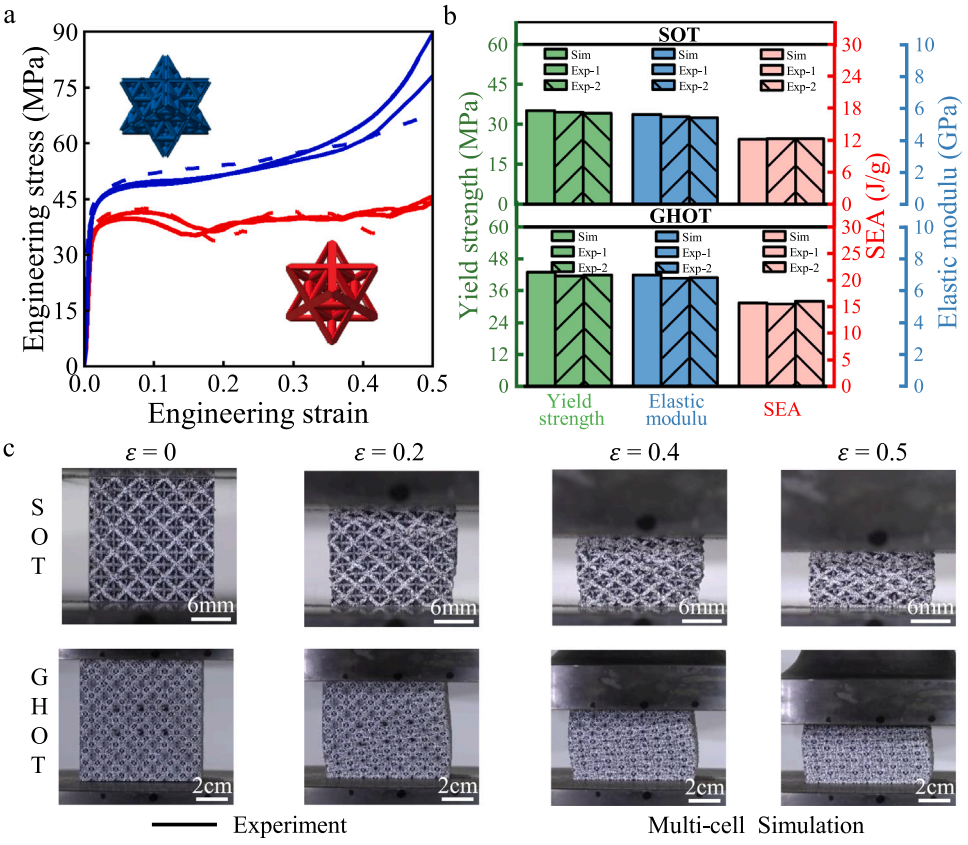

Fig. 10. (a) Uniaxial compression response of GHOT and SOT lattices at relative densities of about 0.2 obtained from simulations and experiments. (b) A direct comparison between SOT and GHOT lattices regarding Young's modulus, yield strength and SEA. (c) Deformation frames of SOT and GHOT lattices under selected uniaxial strains.

during experiment. Furthermore, it accurately predicts the enhanced nonlinear response and uniform deformation mechanism of the GHOT lattice, which also is confirmed by experiment. This comparison underscores the efficacy of our design strategy, integrating hollow truss elements with a grid distribution, in tailoring stability and enhancing energy absorption capabilities.

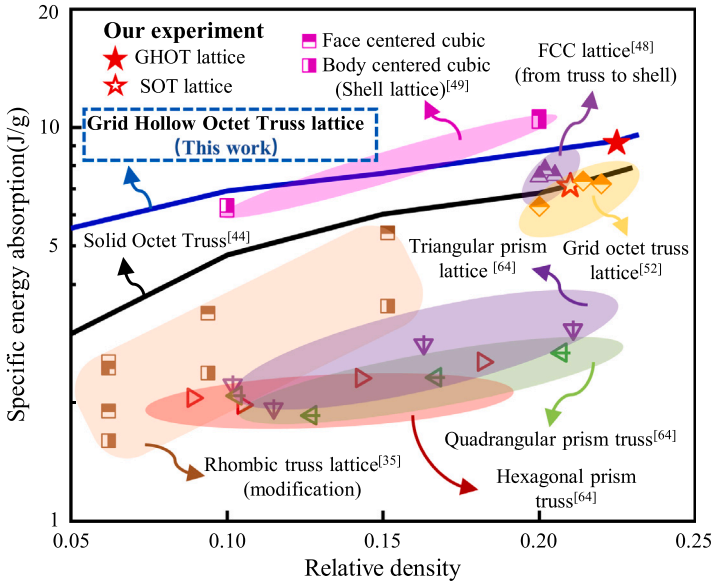

Fig. 11. Ashby charts of specific energy absorption for the proposed structure and other energy-absorbing structures with respect to relative density (Cao et al., 2018; Tancogne-Dejean et al., 2016; Bonatti and Mohr, 2017, 2019b; Zhang et al., 2023; Li et al., 2020).

To further assess the role of the GHOT lattice within the family of energy-absorbing materials, we compared it with other well-known truss, tubular, and shell structures that are dependent on relative density, as shown in Fig. 11. It is evident that the proposed GHOT lattices demonstrate excellent energy absorption efficiency at low and medium relative densities, showing similar SEA values but exhibiting more stable nonlinear responses compared to shell lattices, and surpassing other lattice structures. This superior performance can be attributed to the robust resistance against local and global buckling provided by the integration of hollow trusses and grid distribution, particularly at low relative densities. The tailored stability, combined with high mechanical properties, makes the GHOT lattice a promising candidate for applications in load bearing and energy absorption.

6. Conclusion

Here, we have presented a new class of grid hollow octet truss lattice, achieved by integrating a grid distribution and truss elements into the conventional octet lattice structure, for stability regulation and energy absorption, especially at low relative density. The effective mechanical properties of GOT and GHOT materials have been thoroughly investigated numerically. These properties scale slightly non linearly with relative density and grid number. Specially, the relative elastic modulus and SEA increase with the ratio of inner to outer radius, while the relative yield strength decreases. For instance, at a relative density of 0.2, the relative stiffness of the GHOT lattice ($\alpha = 0.6$) is 1.25 times that of the SOT lattice. At a relative density of 0.05, the SEA of the GHOT lattice ($\alpha = 0.6$) is 1.98 times that of the SOT lattice.

The impact of the ratio of inner to outer radius and grid number on the nonlinear response and deformation mechanism of the octet lattice was comprehensively investigated numerically. Three metrics were proposed to quantitatively assess the stability of low relative density metamaterials. Numerical results indicate that larger α and grid numbers can enhance the stability of the octet lattice by reducing damping tendencies and increasing buckling oscillation periods, particularly at low relative densities. As the relative density increases to 0.1, the integration of grid and hollow structures in the GHOT lattice promotes more uniform deformation, resulting in a stress–strain curve with a nearly zero hardening slope, a characteristic not typically observed in other stretching-dominated truss, shell, and plate lattices. Importantly, GHOT lattices exhibit similar energy absorption capacity but more stable nonlinear responses compared to smooth shell lattices at the same relative density. These findings have been validated through experimental investigation. The tailored stability, combined with high mechanical properties, makes the GHOT lattice a promising candidate for applications in load bearing and energy absorption.

CRediT authorship contribution statement

Peijie Zhang: Writing – original draft, Validation, Methodology, Formal analysis, Data curation, Conceptualization. **Xueyan Chen:** Writing – review & editing, Visualization, Validation, Supervision, Investigation, Funding acquisition, Conceptualization. **Penghui Yu:** Validation, Formal analysis, Data curation. **Kun Zhao:** Validation, Formal analysis, Data curation. **Haoxiang Ma:** Validation, Formal analysis, Data curation. **Shiqiu Liu:** Visualization, Validation, Methodology, Funding acquisition, Formal analysis. **Huifeng Tan:** Writing – review & editing, Validation, Supervision, Funding acquisition, Conceptualization. **Vincent Laude:** Writing – review & editing, Validation, Supervision, Project administration, Investigation. **Muamer Kadic:** Writing – review & editing, Validation, Supervision, Project administration, Methodology, Investigation, Conceptualization.

Declaration of competing interest

The authors declare that they have no known competing financial interests or personal relationships that could have appeared to influence the work reported in this paper.

Acknowledgments

This work was supported by the National Nature Science Foundation of China under Grant No. 12202118, the China Postdoctoral Science Foundation, China (2023M730865), the Heilongjiang Touyan Team (HITTY-20190003) and the Science Foundation of National Key Laboratory of Science and Technology on Advanced Composites in Special Environments, China.

Appendix A. Supplementary data

Supplementary material related to this article can be found online at https://doi.org/10.1016/j.jmps.2025.106068.

Data availability

Data will be made available on request.

References

Al-Ketan, O., Rowshan, R., Al-Rub, R.K.A., 2018. Topology-mechanical property relationship of 3D printed strut, skeletal, and sheet based periodic metallic cellular materials. Addit. Manuf. 19, 167–183.
Ashby, M.F., 2006. The properties of foams and lattices. Philos. Trans. R. Soc. A: Math. Phys. Eng. Sci. 364 (1838), 15–30.
Bauer, J., Meza, L.R., Schaedler, T.A., Schwaiger, R., Zheng, X., Valdevit, L., 2017. Nanolattices: an emerging class of mechanical metamaterials. Adv. Mater. 29 (40), 1701850.
Bonatti, C., Mohr, D., 2017. Large deformation response of additively-manufactured FCC metamaterials: From octet truss lattices towards continuous shell mesostructures. Int. J. Plast. 92, 122–147.
Bonatti, C., Mohr, D., 2019a. Mechanical performance of additively-manufactured anisotropic and isotropic smooth shell-lattice materials: Simulations & experiments. J. Mech. Phys. Solids 122, 1–26.
Bonatti, C., Mohr, D., 2019b. Smooth-shell metamaterials of cubic symmetry: Anisotropic elasticity, yield strength and specific energy absorption. Acta Mater. 164, 301–321.
Cao, X., Duan, S., Liang, J., Wen, W., Fang, D., 2018. Mechanical properties of an improved 3D-printed rhombic dodecahedron stainless steel lattice structure of variable cross section. Int. J. Mech. Sci. 145, 53–63.
Cao, X., Xiao, D., Li, Y., Wen, W., Zhao, T., Chen, Z., Jiang, Y., Fang, D., 2020a. Dynamic compressive behavior of a modified additively manufactured rhombic dodecahedron 316L stainless steel lattice structure. Thin-Walled Struct. 148, 106586.
Cao, X., Zhang, D., Liao, B., Fang, S., Liu, L., Gao, R., Li, Y., 2020b. Numerical analysis of the mechanical behavior and energy absorption of a novel P-lattice. Thin-Walled Struct. 157, 107147.
Chen, X., Laforge, N., Ji, Q., Tan, H., Liang, J., Ulliac, G., Moughames, J., Adrar, S., Laude, V., Kadic, M., 2020a. Introduction to mechanical metamaterials and their effective properties. C. R. Phys. 21 (7–8), 751–765.
Chen, X., Moughames, J., Ji, Q., Martínez, J.A.I., Tan, H., Adrar, S., Laforge, N., Cote, J.-M., Euphrasie, S., Ulliac, G., et al., 2020b. Optimal isotropic, reusable truss lattice material with near-zero Poisson's ratio. Extrem. Mech. Lett. 41, 101048.
Chen, X., Moughames, J., Ji, Q., Martínez, J.A.I., Tan, H., Ulliac, G., Laude, V., Kadic, M., 2022. 3D lightweight mechanical metamaterial with nearly isotropic inelastic large deformation response. J. Mech. Phys. Solids 169, 105057.
Chen, X., Tan, H., 2018. An effective length model for octet lattice. Int. J. Mech. Sci. 140, 279–287.
Chen, X., Yu, P., Ma, H., Zhang, P., Ding, C., Liu, S., Zhang, X., Tan, H., 2024. A class of elastic isotropic plate lattice materials with near-isotropic yield stress. Acta Mater. 120085.
Coulais, C., Sounas, D., Alu, A., 2017. Static non-reciprocity in mechanical metamaterials. Nature 542 (7642), 461–464.
Cummer, S.A., Christensen, J., Alù, A., 2016. Controlling sound with acoustic metamaterials. Nat. Rev. Mater. 1 (3), 1–13.
Deshpande, V., Ashby, M., Fleck, N., 2001a. Foam topology: bending versus stretching dominated architectures. Acta Mater. 49 (6), 1035–1040.
Deshpande, V.S., Fleck, N.A., Ashby, M.F., 2001b. Effective properties of the octet-truss lattice material. J. Mech. Phys. Solids 49 (8), 1747–1769.
Deubel, M., Von Freymann, G., Wegener, M., Pereira, S., Busch, K., Soukoulis, C.M., 2004. Direct laser writing of three-dimensional photonic-crystal templates for telecommunications. Nat. Mater. 3 (7), 444–447.
Duan, S., Wen, W., Fang, D., 2020. Additively-manufactured anisotropic and isotropic 3D plate-lattice materials for enhanced mechanical performance: Simulations & experiments. Acta Mater. 199, 397–412.
Dudek, K.K., Iglesias Martínez, J.A., Ulliac, G., Hirsinger, L., Wang, L., Laude, V., Kadic, M., 2023. Micro-scale mechanical metamaterial with a controllable transition in the Poisson's ratio and band gap formation. Adv. Mater. 35 (20), 2210993.
Florijn, B., Coulais, C., van Hecke, M., 2014. Programmable mechanical metamaterials. Phys. Rev. Lett. 113 (17), 175503.
Frenzel, T., Findeisen, C., Kadic, M., Gumbsch, P., Wegener, M., 2016. Tailored buckling microlattices as reusable light-weight shock absorbers.. Adv. Mater. (Deerfield Beach Fla.) 28 (28), 5865–5870.
Guell Izard, A., Bauer, J., Crook, C., Turlo, V., Valdevit, L., 2019. Ultrahigh energy absorption multifunctional spinodal nanoarchitectures. Small 15 (45), 1903834.
Hamzehei, R., Bodaghi, M., Iglesias Martinez, J.A., Ji, Q., Ulliac, G., Kadic, M., Wang, C., Zolfagharian, A., Wu, N., 2023. Parrot beak-inspired metamaterials with friction and interlocking mechanisms 3D/4D printed in micro and macro scales for supreme energy absorption/dissipation. Adv. Eng. Mater. 25 (11), 2201842.
Han, L., Che, S., 2018. An overview of materials with triply periodic minimal surfaces and related geometry: from biological structures to self-assembled systems. Adv. Mater. 30 (17), 1705708.
Hewage, T., Alderson, K., Alderson, A., Scarpa, F., 2016. Double-negative mechanical metamaterials displaying simultaneous negative stiffness and negative Poisson's ratio properties. Adv. Mater. 28 (46), 10323–10332.

Hooshmand-Ahoor, Z., Luo, H., Danas, K., 2024. M-Voronoi and other random open and closed-cell elasto-plastic cellular materials: Geometry generation and numerical study at small and large strains. Int. J. Solids Struct. 290, 112680.
Hooshmand-Ahoor, Z., Tarantino, M., Danas, K., 2022. Mechanically-grown morphogenesis of Voronoi-type materials: Computer design, 3D-printing and experiments. Mech. Mater. 173, 104432.
Jiang, B., Chen, X., Yu, J., Zhao, Y., Xie, Z., Tan, H., 2022. Energy-absorbing properties of thin-walled square tubes filled with hollow spheres. Thin-Walled Struct. 180, 109765.
Kadic, M., Bückmann, T., Stenger, N., Thiel, M., Wegener, M., 2012. On the practicability of pentamode mechanical metamaterials. Appl. Phys. Lett. 100 (19).
Köhnen, P., Haase, C., Bültmann, J., Ziegler, S., Schleifenbaum, J.H., Bleck, W., 2018. Mechanical properties and deformation behavior of additively manufactured lattice structures of stainless steel. Mater. Des. 145, 205–217.
Laforge, N., Wiltshaw, R., Craster, R.V., Laude, V., Iglesias Martínez, J.A., Dupont, G., Guenneau, S., Kadic, M., Makwana, M.P., 2021. Acoustic topological circuitry in square and rectangular phononic crystals. Phys. Rev. Appl. 15 (5), 054056.
Lakes, R., Wojciechowski, K., 2008. Negative compressibility, negative Poisson's ratio, and stability. Phys. Status Solidi (B) 245 (3), 545–551.
Latture, R.M., Rodriguez, R.X., Holmes, Jr., L.R., Zok, F.W., 2018. Effects of nodal fillets and external boundaries on compressive response of an octet truss. Acta Mater. 149, 78–87.
Li, S., 2008. Boundary conditions for unit cells from periodic microstructures and their implications. Compos. Sci. Technol. 68 (9), 1962–1974.
Li, C., Lei, H., Liu, Y., Zhang, X., Xiong, J., Zhou, H., Fang, D., 2018. Crushing behavior of multi-layer metal lattice panel fabricated by selective laser melting. Int. J. Mech. Sci. 145, 389–399.
Li, C., Lei, H., Zhang, Z., Zhang, X., Zhou, H., Wang, P., Fang, D., 2020. Architecture design of periodic truss-lattice cells for additive manufacturing. Addit. Manuf. 34, 101172.
Li, X., Yu, X., Chua, J.W., Lee, H.P., Ding, J., Zhai, W., 2021. Microlattice metamaterials with simultaneous superior acoustic and mechanical energy absorption. Small 17 (24), 2100336.
Liu, H., Chng, Z.X.C., Wang, G., Ng, B.F., 2021. Crashworthiness improvements of multi-cell thin-walled tubes through lattice structure enhancements. Int. J. Mech. Sci. 210, 106731.
Liu, W., Janbaz, S., Dykstra, D., Ennis, B., Coulais, C., 2024. Harnessing plasticity in sequential metamaterials for ideal shock absorption. Nature 1–6.
Messner, M.C., Barham, M.I., Kumar, M., Barton, N.R., 2015. Wave propagation in equivalent continuums representing truss lattice materials. Int. J. Solids Struct. 73, 55–66.
Meza, L.R., Phlipot, G.P., Portela, C.M., Maggi, A., Montemayor, L.C., Comella, A., Kochmann, D.M., Greer, J.R., 2017. Reexamining the mechanical property space of three-dimensional lattice architectures. Acta Mater. 140, 424–432.
Mohr, D., 2005. Mechanism-based multi-surface plasticity model for ideal truss lattice materials. Int. J. Solids Struct. 42 (11–12), 3235–3260.
Oudich, M., Kong, X., Zhang, T., Qiu, C., Jing, Y., 2024. Engineered Moiré photonic and phononic superlattices. Nat. Mater. 23 (9), 1169–1178.
Portela, C.M., Greer, J.R., Kochmann, D.M., 2018. Impact of node geometry on the effective stiffness of non-slender three-dimensional truss lattice architectures. Extrem. Mech. Lett. 22, 138–148.
Schaedler, T.A., Jacobsen, A.J., Torrents, A., Sorensen, A.E., Lian, J., Greer, J.R., Valdevit, L., Carter, W.B., 2011. Ultralight metallic microlattices. Sci. 334 (6058), 962–965.
Song, J., Zhou, W., Wang, Y., Fan, R., Wang, Y., Chen, J., Lu, Y., Li, L., 2019. Octet-truss cellular materials for improved mechanical properties and specific energy absorption. Mater. Des. 173, 107773.
Tan, X., Li, Y., Wang, L., Yao, K., Ji, Q., Wang, B., Laude, V., Kadic, M., 2023. Bioinspired flexible and programmable negative stiffness mechanical metamaterials. Adv. Intell. Syst. 5 (6), 2200400.
Tan, X., Martínez, J.A.I., Ulliac, G., Wang, B., Wu, L., Moughames, J., Raschetti, M., Laude, V., Kadic, M., 2022a. Single-step-lithography micro-stepper based on frictional contact and chiral metamaterial. Small 18 (28), 2202128.
Tan, X., Wang, B., Chen, S., Zhu, S., Sun, Y., 2019. A novel cylindrical negative stiffness structure for shock isolation. Compos. Struct. 214, 397–405.
Tan, X., Wang, L., Zhu, S., Chen, S., Wang, B., Kadic, M., 2022b. A general strategy for performance enhancement of negative stiffness mechanical metamaterials. Eur. J. Mech. A Solids 96, 104702.
Tancogne-Dejean, T., Diamantopoulou, M., Gorji, M.B., Bonatti, C., Mohr, D., 2018. 3D plate-lattices: an emerging class of low-density metamaterial exhibiting optimal isotropic stiffness. Adv. Mater. 30 (45), 1803334.
Tancogne-Dejean, T., Li, X., Diamantopoulou, M., Roth, C., Mohr, D., 2019. High strain rate response of additively-manufactured plate-lattices: experiments and modeling. J. Dyn. Behav. Mater. 5, 361–375.
Tancogne-Dejean, T., Mohr, D., 2018. Elastically-isotropic elementary cubic lattices composed of tailored hollow beams. Extrem. Mech. Lett. 22, 13–18.
Tancogne-Dejean, T., Spierings, A.B., Mohr, D., 2016. Additively-manufactured metallic micro-lattice materials for high specific energy absorption under static and dynamic loading. Acta Mater. 116, 14–28.
Tarantino, M., Zerhouni, O., Danas, K., 2019. Random 3D-printed isotropic composites with high volume fraction of pore-like polydisperse inclusions and near-optimal elastic stiffness. Acta Mater. 175, 331–340.
Wang, L., Ulliac, G., Wang, B., Iglesias Martínez, J.A., Dudek, K.K., Laude, V., Kadic, M., 2022. 3D auxetic metamaterials with elastically-stable continuous phase transition. Adv. Sci. 9 (34), 2204721.
Yang, H., D'Ambrosio, N., Liu, P., Pasini, D., Ma, L., 2023. Shape memory mechanical metamaterials. Mater. Today 66, 36–49.
Yu, P., Zhang, P., Ji, Q., Yang, F., Tan, X., Chen, X., Tan, H., Laude, V., Kadic, M., 2024. A multi-step auxetic metamaterial with instability regulation. Int. J. Solids Struct. 113040.
Zhang, P., Yu, P., Zhang, R., Chen, X., Tan, H., 2023. Grid octet truss lattice materials for energy absorption. Int. J. Mech. Sci. 259, 108616.
Zhao, Y., Belkin, M., Alù, A., 2012. Twisted optical metamaterials for planarized ultrathin broadband circular polarizers. Nat. Commun. 3 (1), 870.
Zhao, M., Zhang, D.Z., Li, Z., Zhang, T., Zhou, H., Ren, Z., 2022. Design, mechanical properties, and optimization of BCC lattice structures with taper struts. Compos. Struct. 295, 115830.
Zheng, X., Lee, H., Weisgraber, T.H., Shusteff, M., DeOtte, J., Duoss, E.B., Kuntz, J.D., Biener, M.M., Ge, Q., Jackson, J.A., et al., 2014. Ultralight, ultrastiff mechanical metamaterials. Sci. 344 (6190), 1373–1377.
Zhu, S., Wang, J., Chen, L., Liu, T., Li, W., 2024. Negative stiffness metamaterial with directional stability in uniform fields. Thin-Walled Struct. 194, 111302.